Next generation high resolution perovskite direct conversion detector: Monte Carlo design optimisation and virtual clinical trial

J O'Connell, S Kundu, M Saidaminov and M Bazalova-Carter

2023

IOP Publishing Phys. Med. Biol. 68 (2023) 025016 https://doi.org/10.1088/1361-6560/acae15

Physics in Medicine & Biology

IPEM Institute of Physics and Engineering in Medicine

PAPER

Next generation high resolution perovskite direct conversion detector: Monte Carlo design optimisation and virtual clinical trial

J O'Connell, S Kundu, M Saidaminov and M Bazalova-Carter

University of Victoria, 3800 Finnerty Road, Victoria, Canada, V8P 5C2, Canada

E-mail: jerichoo@uvic.ca

Keywords: perovskite, CT, CBCT, VCT, detector, mammography

OPEN ACCESS

RECEIVED
7 September 2022

REVISED
1 December 2022

ACCEPTED FOR PUBLICATION
22 December 2022

PUBLISHED
11 January 2023

Abstract

We implement virtual clinical integration of next-generation perovskite detectors into common x-ray imaging devices. This was achieved by performing Monte Carlo (MC) optimisation of the design and benchmarking of low cost, high spatial resolution, direct conversion perovskite crystal x-ray flat panel imagers for a next generation of breast-, MV-, and kV-cone beam CT detectors. Semiconductor methylammonium lead bromide perovskite crystals energy deposition efficiencies calculated in TOPAS were benchmarked against four common detector materials for twelve detector crystal thicknesses between 40 to 15 mm and ten beam energies ranging from 20 keV to 6 MeV. Based on these simulations, Koning's dedicated breast CT, and Varian's Truebeam kV- and MV-cone beam CT systems were designated as suitable applications for perovskite detectors. System specific Fastcat hybrid MC cone beam CT image simulation was subsequently used to optimise the perovskite detector design and conduct virtual clinical trials. Device-specific optimal perovskite crystal thicknesses were calculated to be 0.30, 0.86, and 1.99 mm for Koning breast CT and Truebeam kV- and MV-cone beam CT systems, respectively. Replacing the current detectors on these machines with low cost perovskite crystal detectors could be advantageous as it would simultaneously yield 12.1%, 9.5% and 86.1% improvements in detective quantum efficiency as well as increases in contrast to noise ratio in brain, lung, and bone tissues.

1. Introduction

Recent developments in perovskite crystal material chemistry have for the first time introduced a detector material that is simultaneously low-cost, high atomic number, and direct conversion, a combination which could power a next generation of high performing x-ray detectors. These detectors have been demonstrated to have superior spatial resolution to existing detectors, especially at large detector crystal thicknesses (Datta *et al* 2021): even though spatial resolution tends to decrease with thickness, a 1200 μm perovskite crystal detector showed higher modulation transfer function (MTF) than amorphous selenium (a-Se) of any thickness (Datta *et al* 2021).

Additionally, perovskite crystals such as methylammonium lead bromide ($MAPbBr_3$) have excellent material chemistry when it comes to x-ray detection: the combination of perovskite's high charge carrier mobility (μ) and long carrier lifetimes (τ), as defined by the $\mu\tau$ product, makes them very sensitive to incident x-ray photons (Yakunin *et al* 2015, Wei *et al* 2016, Kim *et al* 2017, Safa Kasap 2017, Shrestha *et al* 2017, Huang *et al* 2019, Ye *et al* 2019, Dennis *et al* 2021). The $\mu\tau$ product of some perovskite crystals is equivalent to that of cadmium zinc telluride (CZT) a promising material that is already being used in cutting edge medical imaging applications (Yakunin *et al* 2015, Wei *et al* 2016, Kim *et al* 2017, Safa Kasap 2017, Shrestha *et al* 2017, Huang *et al* 2019, Ye *et al* 2019, Dunning *et al* 2020), while perovskite is simultaneously cheaper and easier to manufacture than CZT (Yakunin *et al* 2015). Thus, it is anticipated that this technology could bring in a new generation of flat-panel x-ray detectors.

Analogously, with the introduction of the first generation of direct conversion digital amorphous selenium (a-Se) detectors in the 1990s, a large theoretical and experimental body of work was created to characterise these detectors and their applications (Papin and Huang 1987, Rowlands *et al* 1991, Neitzel *et al* 1994, Que and Rowlands 1995). Que *et al* concluded that geometric distortion from photon incidence at an angle and focal spot were the major contributors to detector MTF. Therefore, as perovskite crystals are produced with large thicknesses it is important to consider the effect of geometric MTF degradation which dominates the spatial resolution of flat panel detectors, especially for CT and MV cone beam CT (CBCT) where the higher energy x-rays penetrate deeper in the detector. Additionally, the finite focal spot size for CT modalities limits achievable detective quantum efficiency in flat panels detectors, which is an engineering constraint on the system and cannot be reduced arbitrarily due to heat dissipation requirements in CT. Thus, it is important to discuss the benefit of perovskite detectors while considering these constraints. As a thick high spatial resolution perovskite detector may provide limited benefit over a traditional detector if the system spatial resolution is limited by geometric effects and focal spot blur rather than actual detector spatial resolution.

So, although the high sensitivity and superior spatial resolution of perovskite detectors has been demonstrated in the literature, no quantification has been done on whether these improvements translate to improvements in medical imaging. In this work first we optimise detector thickness based on a combination of theoretical models and Monte Carlo (MC) simulations taking into account degradation of spatial resolution due to geometric factors and device focal spot sizes. Further we perform virtual clinical trials (VCTs) on anthropomorphic phantoms using device specifications from three common CBCT devices to demonstrate the improvement associated with next generation perovskite detectors.

2. Materials and methods

2.1. Energy deposition efficiency (EDE)

To determine the domains of medical imaging for which perovskite crystals are most suited, the EDE of perovskite crystals was compared to other common medical imaging materials for a wide range of photon energies used in medical imaging. EDE, η_e, is a measure of the fraction of the energy absorbed in the detector relative to the energy incident on the detector and is a robust measure of the potential efficiency of a detector. At an energy e, η_e, is defined in terms of ratio of the incident energy $E_{e,i}$ on the detector to the energy absorbed in the detector crystal $E_{e,\mathrm{abs}}$ from a mono-energetic pencil beam at energy e impinging normally to the detector

$$\eta_e = \frac{E_{e,\mathrm{abs}}}{E_{e,i}}. \tag{1}$$

Simulations of detector EDE were performed in TOPAS (Perl *et al* 2012) with 10^7 initial particles per energy per crystal thickness. The mono-energetic pencil beam energies used were 10 to 90 keV in 10 keV increments, 100 to 900 keV in 100 keV increments, and 1, 2, 4, and 6 MeV. A greater emphasis of energies in the low energy range was used to help resolve photo-electric behaviour near the K-edges of the detector constituent elements. Detector thicknesses of 0.029, 0.1, 0.2, 0.3, 0.5, 1, 2, 5, 10, and 15 mm were considered. A global particle range cutoff of 0.001 mm was used to remain much smaller than the minimum studied crystal thickness of 0.029 mm. Simulations were run on a linux desktop computer on eight 4.0 GHz Intel Skylake cores with compute times on the order of 30 min. This aforementioned desktop environment and particle cutoff were used in all simulations in this work if not specified.

2.2. Detector materials

Energy deposition efficiency was calculated for three common detector materials; amorphous selenium (a-Se), caesium iodide (CsI), and gadolinium oxysulphide (GOS). a-Se is a common material used for mammography and lower energy imaging application, columnar CsI is standard detector material for kV CT imaging, and GOS is a low cost material commonly used in kV and MV imaging systems. Additionally, cadmium zinc-telluride (CZT) detector was modelled, although not as commonly used, CZT is a promising high atomic number direct conversion material that has properties similar to perovskite halides and is used for photon-counting CT imaging.

The detectors used in the EDE comparison were modelled based on material specifications of existing detectors. As such, the density of the Cu-GOS detector is the density of the phosphor and binder glue of a Varian aS1200 detector, while the CsI detector's density is the average density of a PaxScan 4030CB with a 70% fill ratio. The CZT detector is based on material compositions from Redlen (Redlen Technologies, Saanichton, BC, Canada) (Dunning *et al* 2020, Richtsmeier *et al* 2020). Additional material information is shown in table 1. All detectors were modelled with a pixel pitch of 100 μm.

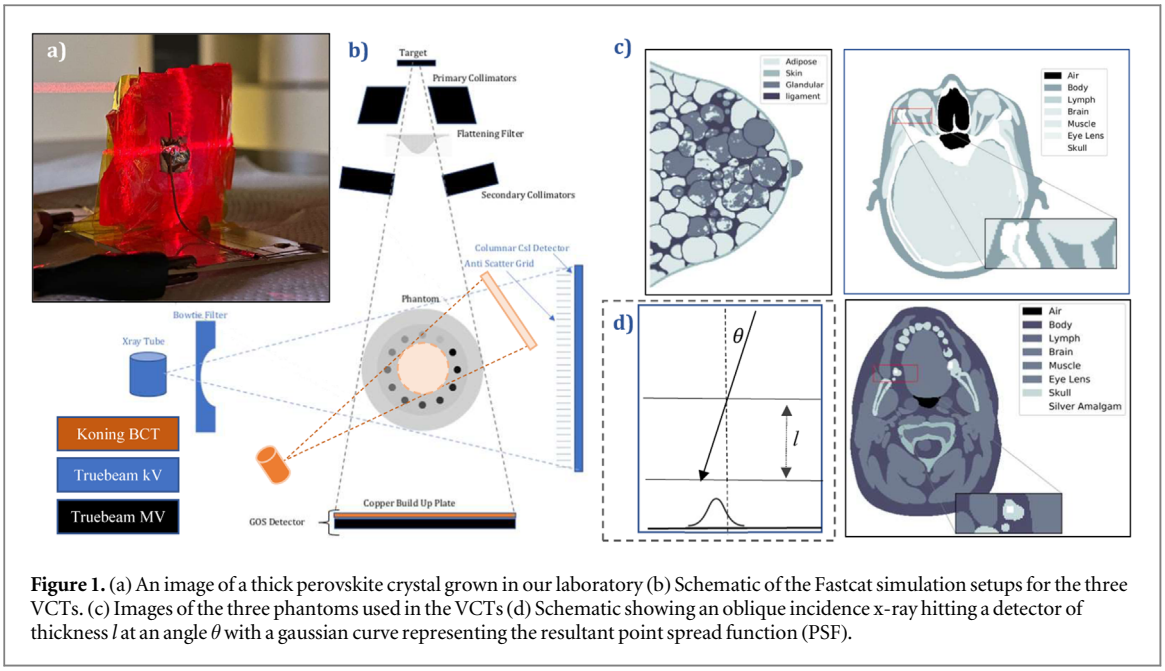

Figure 1. (a) An image of a thick perovskite crystal grown in our laboratory (b) Schematic of the Fastcat simulation setups for the three VCTs. (c) Images of the three phantoms used in the VCTs (d) Schematic showing an oblique incidence x-ray hitting a detector of thickness l at an angle θ with a gaussian curve representing the resultant point spread function (PSF).

Table 1. Detector parameters.

Material	Chemical Formula	Density [g cm^{-3}]	Direct Conversion	Columnar	K-edges [keV]	μ 40 keV [cm^{-1}]	μ 100 keV [cm^{-1}]	μ 1 MeV [cm^{-1}]
Perovskite	$MAPbBr_3$	3.83	Yes/No	No	13.5 (Br) 88.0 (Pb)	29.9	9.87	0.29
Cu-GOS	Gd_2O_2S:Tb	4.59	No	No	50.2 (Gd) 52.0 (Tb)	16.2	7.30	0.25
CsI	CsI:Tl	3.16	No	Yes	36.0 (Cs) 85.5 (Tl)	72.5	6.42	0.18
aSe	Se	4.26	Yes	No	12.7 (Se)	32.3	2.80	0.25
CZT	CdZnTe	5.8	Yes	No	26.7 (Cd) 31.8 (Te)	104	9.05	0.33

Table 2. VCT parameters.

Imaging Machine	SAD–SID [mm]	Incidence Angle [°]	Detector – Crystal thickness	Beam kVp [kV]	Beam Filtration	Focal Spot Nominal [mm]
Koning BCT	422–778	7.24	PaxScan 4030CB (CsI:Tl)–0.6 mm	49	0.8 mm Be, 1.58 mm Al	0.3
Varian kV CBCT	1000–1500	6	PaxScan 4030CB (CsI:Tl)–0.6 mm	100	3 mm Al, 0.89 mm Ti	1.0
Varian MV CBCT	1000–1500	6	aS1200 (Cu-GOS)–0.29 mm	6000	N/A	1.5 (López-Sánchez *et al* 2019)

2.3. Virtual clinical trials

Three VCTs were conducted in this work to demonstrate perovskite's application in different imaging areas: (1) the Koning dedicated breast CT (BCT) (KBCT 1000, Koning Corporation, West Henrietta, NY, USA), (2) the Varian Truebeam Stx (Varian Medical Systems, Palo Alto, CA) kV on board imager (OBI), and (3) the Truebeam electronic portal imager (EPID) for MV CBCT. A description of the device specifications used in the simulations can be found in table 2 and a schematic of the setup in figure 1.

Table 3. Focal spot parameters.

Machine	IEC nominal Focal spot	IEC focal spot Dimensions [mm]	FWHM [mm]	Scaling	s [mm]
Koning BCT	0.3 mm	0.450.6	0.3321	0.81	0.114
Varian kV CBCT	1 mm	1.42.0	1.027	0.5	0.218
Varian MV CBCT	N/A	N/A	1.5	0.5	0.340

2.4. Modulation transfer function

The MTFs in this study were first calculated using Fastcat and degraded based on the extensive theoretical work of Que and Rowlands (1995) who developed a rigorous framework for MTF degradation. Fastcat weights mono-energetic point spread functions calculated using Topas MC to analytically calculate MTFs for polyenergetic beams. Fastcat's full MTF methodology and experimental validation of the MTF calculations can be found in our previous work (O'Connell *et al* 2021). According to Que and Rowlands, geometrical distortion is often the largest contributor to MTF degradation. This is especially true for thick detectors and higher energies where the photons and secondary electrons may travel to large depths in the detector crystals. Geometric MTF distortion can be described using the following equation:

$$\mathrm{MTF}_g(\nu) = \frac{\{[1 - L]^2 + 4L \sin^2(\pi\nu l \tan\theta))\}^{1/2}}{[1 - L][1 + (2\pi\nu \sin\theta/\mu)^2]^{1/2}}, \tag{2}$$

where

$$L = \exp(-\mu l/\cos\theta) \tag{3}$$

and μ is the attenuation coefficient of the detector material at a given energy. In the case of a polyenergetic beam the attenuation was weighted by the fluence, detector EDE, and energy. The weighting by the detector EDE and energy was necessary as these factors influence the readout intensity of an energy integrating detector. l is the thickness of the detector while θ is the angle of the incidence of the photons. Finally, ν is the spatial frequency of the MTF. A schematic of geometric distortion can be seen in figure 1(d).

For the flat panel detectors discussed, the photon incidence angle, θ, was approximated to be the mean angle of incidence for a typical acquisition. A value of 7.24° was calculated as the mean angle of incidence for the BCT. In kV- and MV-CBCT the average angle of incidence was estimated to be 6°, corresponding to half the angle of the detector collimation of 12°.

The second contributor to MTF degradation discussed is the focal spot of the x-ray tube. It is defined as the full width at half maximum (FWHM) of the source intensity on the x-ray tube target surface. The focal spots of the machines were approximated as Gaussian point spread functions (PSF). Taking the Fourier transform of a Gaussian we obtain the focal spot MTF (MTF_{fs}) which is also a Gaussian of the form:

$$\mathrm{MTF}_{fs}(\nu) = \exp(-\pi^2\nu^2 s^2), \tag{4}$$

where s is the inverse of the standard deviation of the point spread function and ν is the spatial frequency.

Nominal focal spots as defined by the IEC 60336:2005 standard are stated in table 3. According to the standard, the full width 15% max is used as the measure of the focal spot. The nominal focal spot sizes are not exact and have associated permissible dimensions according to the IEC standard. The average of the width and length of the focal spot is averaged and approximated by a gaussian of that dimension. Based on this gaussian, one can calculate a value for the standard deviation s. For the Koning BCT 0.3 nominal focal spot value the permissible dimensions are a width of 0.45 mm and a length of 0.65 mm and for the Truebeam kV-OBI the 1.0 nominal focal spot value the permissible dimensions are a width of 1.4 mm and a length of 2.0 mm. For the Truebeam the MV beam the dimensions relate directly to the FWHM (López-Sánchez *et al* 2019). Using a gaussian distribution these measurements are related to the standard deviation s: a full width at 15% max is 3.894s and the FWHM is 2.355s. These values are then multiplied by the scaling factor, which is the ratio of the source-imager distance (SID) minus the source-axis distance (SAD) divided by the SAD.

The partial MTFs, which are Fourier transforms of spatial convolutions, are then multiplied in the frequency domain to generate a final MTF resultant from the original MTFs degraded by focal spot and geometric distortions.

2.5. Noise power spectrum (NPS)

The NPS for each of the detector crystal thicknesses was calculated using MC techniques with the Fastcat hybrid MC code (O'Connell *et al* 2021, O'Connell and Bazalova-Carter 2021). For each photon beam and detector thickness, a flat-field image was simulated in compliance with the IEC-defined normal exposure. The detector was irradiated with an approximate exposure of 1×10^{-7} C kg^{-1} and a 128 × 128 pixel area of the detector was

used for calculation of the NPS. The NPS analysis component was the IEC RQA5 method as described by Dobbins *et al* (2006). The NPS is defined as the Fourier amplitude of a two dimensional image with intensity I as

$$\mathrm{NPS}(\mu_n, \nu_k) = \lim_{N_x,\, N_y \to \infty} (N_x N_y \Delta x \Delta y) |\mathcal{F}_{n,k}[I(x, y) - \bar{I}]|^2. \tag{5}$$

Where $I(x, y)$ is the image intensity at the pixel location (x, y), $\mathcal{F}_{n,k}$ is the two dimensional Fourier transform where n and k are indices for the specific spatial frequency being sampled, $\bar{I}$ is the mean intensity of the image, ν and μ are the spatial frequencies conjugate to x and y, while Δx and Δy are the pixel pitch of the detector and N_x, N_y are the number of pixels in the x and y direction, respectively. Two dimensional NPS was calculated using the IEC 62220-1 method; a 640 $\times$640 pixel area of the detector was evaluated with 256 $\times$ 256 overlapping regions of interest (ROIs). Second order detrending was used as a background subtraction method and seven central rows of the two dimensional NPS above and below the x-axis were combined to produce a one dimensional NPS.

2.6. Detective quantum efficiency

The detective quantum efficiency (DQE) of a detector is a metric that measures the degradation of the information contained in an output signal relative to the original input signal. Since detectors have physical limitations determined by Poisson statistics and finite pixel size, the DQE is measured relative to the ideal detector which is only limited by these factors. The work of Ranger *et al* was followed to calculate the DQE (Ranger *et al* 2007). Formally DQE is calculated as:

$$\mathrm{DQE}(\nu) = S^2 \frac{\mathrm{MTF}^2(\nu)}{\mathrm{NPS}(\nu) \times q \times E} = \frac{\mathrm{MTF}^2(\nu)}{\mathrm{NNPS}(\nu) \times q \times E}. \tag{6}$$

Where MTF(ν) is the frequency-dependent MTF, NPS(ν) is the frequency-dependent NPS, S is the square of the large-area signal intensity. This equation can be simplified by using the NNPS which is the NPS divided by the large-are signal intensity squared. Meanwhile, the q value is an estimate of the number of incident x-ray photons per unit area per unit of exposure incident on the detector generally estimated through computer modelling. Finally, E is the IEC-defined normal exposure. q values and normal exposures were not calculated in this work since they were constant as a function of detector crystal thicknesses, making them unimportant in the context of a detector thickness optimization. Thus as measure denoted the relative DQE ($\mathrm{DQE_r}$) was used

$$\mathrm{DQE_r}(\nu) = \frac{\mathrm{MTF}^2(\nu)}{\mathrm{NNPS}(\nu)}. \tag{7}$$

2.7. Imaging beams

Each imaging task was simulated with an appropriate x-ray beam. The BCT spectra was modelled after 40 kVp beam with 0.8 mm of beryllium filtration and 2 mm aluminum filtration. The kV CBCT 100 kVp beam was modelled with 3 mm inherent aluminum filtration and a 0.89 mm thick titanium beam hardening filter. The x-ray beam spectra were simulated in Fastcat by means of xpecgen (Hernández and Fernández 2016). In addition, a 6 MV photon energy spectra was calculated from the Truebeam MV phasespace file provided by Varian and available online through the IAEA NDS (Capote 2023).

2.8. Phantoms

VCTs for each of the three imaging systems were conducted using appropriate phantoms depicted in figure 1(c). BCT images of an anthropomorphic breast phantom with microcalcifications (Jeon *et al* 2017) were simulated for the Koning BCT setup. The breast phantom was composed of adipose tissue, skin, and glandular tissue, with the microcalcification composed of cortical bone. Material elemental compositions were defined using the values defined in the Geant4 default materials (Bert *et al* 2013) and ICRU 44 (Woodard and White 1986). The kV and MV CBCT VCTs featured an XCAT (Segars 2010) head phantom. The kV image demonstrated the image quality in the brain while the MV image focused on a region in the skull with silver amalgam fillings that would generate streaking artifacts in kV images.

2.9. Image generation and reconstruction

Virtual clinical trial CBCTs were simulated using the Fastcat hybrid MC code. Fastcat uses an angularly independent scatter approximation to speed up the CBCT image simulations in rotationally symmetric objects. Fastcat simulations consider the physics processes described by the Topas Penelope physics module as well as the Topas optical module for simulating light transport in scintillators. Fastcat simulations closely agree with experimental MTF and NPS measurements on a Truebeam linac for both the Cu-GOS electronic portal imager (EPID) and CsI on-board imager (OBI) (O'Connell *et al* 2021). Fastcat's full MTF methodology and experimental validation of the MTF calculations can be found in O'Connell and Bazalova's previous work

Table 4. Phantom parameters.

Phantom	# of pixels [x, y, z]	Dimensions [x, y, z] [mm^3]
BCT	512, 512, 156	205, 205, 125
kV CBCT (XCAT)	1024, 1024, 256	512, 512, 31.25
MV CBCT (XCAT)	1024, 1024, 256	512, 512, 31.25

(O'Connell *et al* 2021, O'Connell and Bazalova-Carter 2021). MTF values for the Paxscan CB4030 and aS1200 detectors agreed within 4.2% and 2.5% of experimental measurements, respectively. All phantom parameters as specified in Fastcat are summarized in tables 2 and 4. To generate CBCT images, views were acquired at 300, 887, and 493 equally spaced angles between 0° and 360° for the BCT, kV- and MV-CBCT acquisitions, respectively. Images were reconstructed using the FDK algorithm (Feldkamp *et al* 1984) with a Ram-Lak filter. All scans were simulated to have noise consistent with a 7 mGy mean dose to the phantom. Doses were calculated in Fastcat. CBCT image simulations took, on average, 64 to 87 s on a Nvidia GeForce RTX 2070 GPU (Nvidia Corp., Santa Clara, CA).

CBCT image contrast to noise ratio (CNR) was compared between perovskite and the default detector using the same ROIs in each image. Contrast was measured against adipose tissue in reconstructions of the breast phantom and muscle in reconstructions of the head phantom. We denote the average HU value from this region μ_{body} and the value from the insert μ_{ROI}. CNR was measured relative to the same region using the standard deviations σ_{ROI} and σ_{body} as

$$\mathrm{CNR} = \frac{\mu_{ROI} - \mu_{body}}{\sqrt{\sigma_{body}^2 + \sigma_{ROI}^2}}. \tag{8}$$

CNR was bootstrapped to generate a 99% confidence interval.

3. Results

3.1. Energy deposition efficiency

The EDE as a function of beam energy and detector thickness for both the perovskite $MAPbBr_3$ material and a variety of other materials is presented in figure 2. The perovskite EDE is also compared individually to current detector materials. The perovskite material's high atomic number lead allows for greater EDE than a-Se at all energies and thicknesses, with a greater than 60% increase generally above the K-edge of lead and a 20%–30% efficiency increase for low thickness detectors at low energies. As compared to CsI, perovskite EDE is increased for mammography energies below the K-edges of caesium at 36 keV and iodine at 33 keV while CsI has 20%–30% better EDE in the 30–80 keV range, with 10%–20% better efficiency above the K-edges of thallium and lead at 85 and 88 keV, respectively. CZT has generally higher EDE than perovskite save in the mammography range below the K-edge of cadmium at 27 keV. GOS is a worse energy absorber than perovskite for energies below the K-edge of gadolinium at 50 keV. Additionally, perovskite is a better energy absorber in the range above the lead K-edge of 88 keV to approximately 1 MeV, which corresponds to the high fluence of an MV x-ray spectrum.

3.2. Detective quantum efficiency

The DQE as a function of crystal thickness and beam angle of incidence are shown in figure 3(a). As expected according to the work of Que *et al* the DQE as a function of thickness was much more affected by angle at higher energies due to geometric MTF degradation (Que and Rowlands 1995). For the 40 kVp beam used for the BCT the detector, DQE decreased by less than 5% after the peak DQE but decreased by a factor of 5 for the MV CBCT at 15 mm thicknesses and an 18 degree angle of incidence. For the specific machine setups studied (figure 3(b)), the optimal DQE thickness for the Koning BCT, and Truebeam MV and kV CBCT were 0.30, 0.86, and 1.99 mm, respectively. Figure 4 shows a comparison between the current DQE_r of the three devices discussed and the DQE_r simulated using a perovskite detector of optimal thickness. The substitution of the optimal perovskite detectors in Koning BCT and Truebeam kV- and MV-CBCT increased DQE_r by 12.1%, 9.5% and 86.1% over current values, respectively.

DQE_r was calculated for each of the three imaging systems using the parameters described in tables 1 and 2 for detector thicknesses of 0.029, 0.1, 0.2, 0.3, 0.5, 1, 2, 5, 10, and 15 mm. DQE_r was then interpolated using radial basis function interpolation to find the crystal thickness corresponding to the maximum DQE_r.

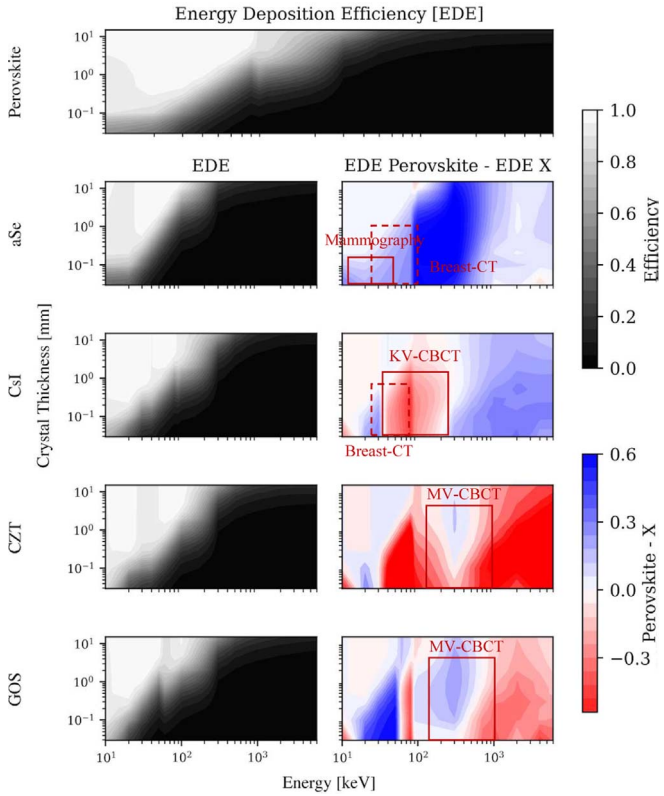

Figure 2. Plots of the EDE as a function of crystal thickness and photon energy for each detector material are shown, logarithmic interpolation was used to generate the surfaces shown in this figure from the discrete energies and thicknesses listed in section 2.1. In the right column the EDE of perovskite is compared to the other detectors, blue regions indicating superior EDE for perovskite while red regions indicate regions where perovskite performs poorer as compared to the existing detector.

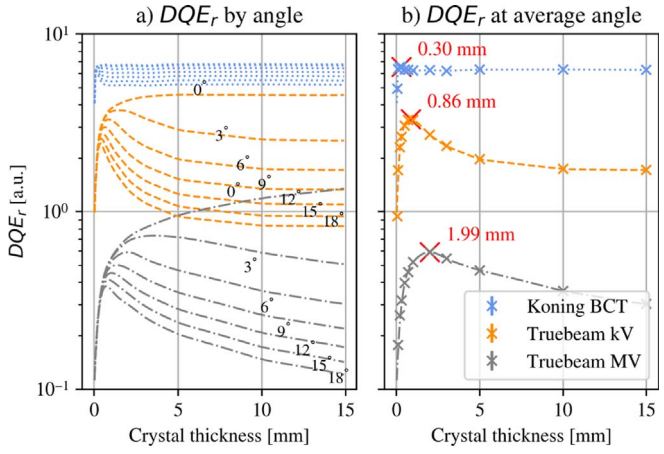

Figure 3. The relative DQE results. (a) Relative DQE averaged over frequencies up to the Nyquist frequency of 5 lp mm^{-1} for a detector pixel pitch of 100 μm was simulated for the different experimental setups at a variety of photon incidence angles as a function of detector thickness. (b) The DQE for each of the experimental setups using the average angle of incidence is shown, the thickness of the maximum relative DQE is shown in red.

3.3. Virtual clinical trial

3.3.1. Koning breast CT

In figure 5 MC-simulated BCT images of the anthropomorphic breast phantom acquired with the default CsI detector (0.30 mm thick, 0.194 mm pixel pitch) and a perovskite detector (0.8 mm thick 0.194 mm pixel pitch) are shown. The perovskite detector resulted in a 87% increase in contrast in the microcalcification of the breast phantom. The CNR in inserts of glandular tissue and bone based showed a 28% decrease and 9.8% increase in CNR, respectively, demonstrating an improvement in microcalcification detection and DQE using the novel perovskite detector which can be manufactured at lower cost than CsI.

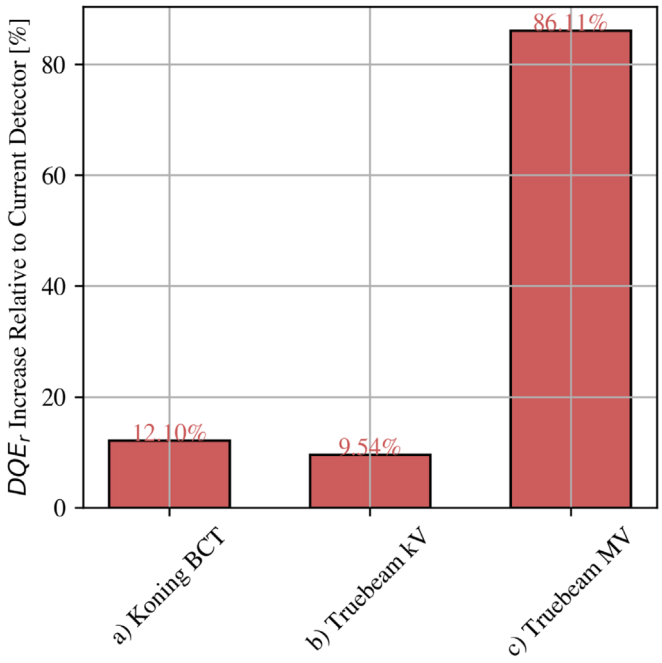

Figure 4. The DQE of the optimal perovskite thickness relative to the default detector for the three experimental setups.

3.3.2. Truebeam kV- and MV-CBCT

VCTs of Varian Truebeam kV- (6) and MV-CBCT (7) images for 0.336 mm pixel pitch, 0.6 mm thick CsI and 0.29 mm thick Cu-GOS detectors and 0.86 mm and 1.99 mm thick 0.336 mm pixel pitch perovskite detectors, respectively, show dramatic image quality improvement for the perovskite detector in the XCAT head phantom. As shown in figures 6(a)–(b), kV-CBCT spatial resolution in fine bone features and tissue contrast was improved dramatically using the perovskite direct conversion detector. At the same time, perovskite detector CNR in brain and skull was increased by 8% and 13%, respectively, as compared to the default CsI detector. In figure 7 the high efficiency of the perovskite detector as compared to the Cu-GOS MV-CBCT resulted in dramatic improvement of CNR in the XCAT head phantom with silver fillings in two molars. CNR in lung and C4-vertebra tissues which are commonly imaged when positioning a patient were improved from 0.8 and 1.1 to 10.3 and 12.0, respectively.

4. Discussion

In the VCTs, perovskite detectors showed great potential to ameliorate existing CBCT devices. We show improvements to CNR in a number of tissues. In figure 5, a breast calcified lesion that is poorly defined using a CsI detector, while the increased spatial resolution and CNR of the perovskite detector led to differentiation of the lesion from the surrounding tissue. This differentiation could lead to more accurate identification of such anatomical structures in breast cancer screening. Additionally, there was a 9.8% improvement in bone CNR for the perovskite detector, however, there was also a decrease in the CNR in glandular tissue. This was likely due to a combination of the higher spatial resolution and the thinner detector increasing the spatial resolution at the cost of increased noise as is the general trade-off. To increase the CNR in glandular tissue we recommend that the detector be made thicker than the 0.3 mm which results in the optimal DQE, for example up to a 1.1 mm detector would greatly increase CNR and reduce DQE by less than 2%. Likewise, the improved contrast in the MV-CBCT when perovskite detector is used shows a metal artifact free image of a human jaw with dental amalgam, an imaging case in which kV-CBCT generally produces large streaking artifacts covering clinically relevant anatomical features. Additionally, the MV-CBCT contrast increase for the perovskite detector relative to the default GOS detector could lead to possible imaging of patients on machines lacking a kV-OBI which is the case for most machines in low- and middle-income countries.

The EDE results yielded better performance for perovskite than all other detectors tested in the mammography range of energies (10–40 keV) and only CZT had superior EDE in the MV imaging energy range (0.5–1.5 MeV). In this work we estimate EDE to be a proxy for DQE(0) or the base absorption of the detector, assuming that the detectors have similar conversion efficiency between energy absorbed and readout signal intensity. We assume this equivalence for simplicity as the electron hole transport inside direct conversion

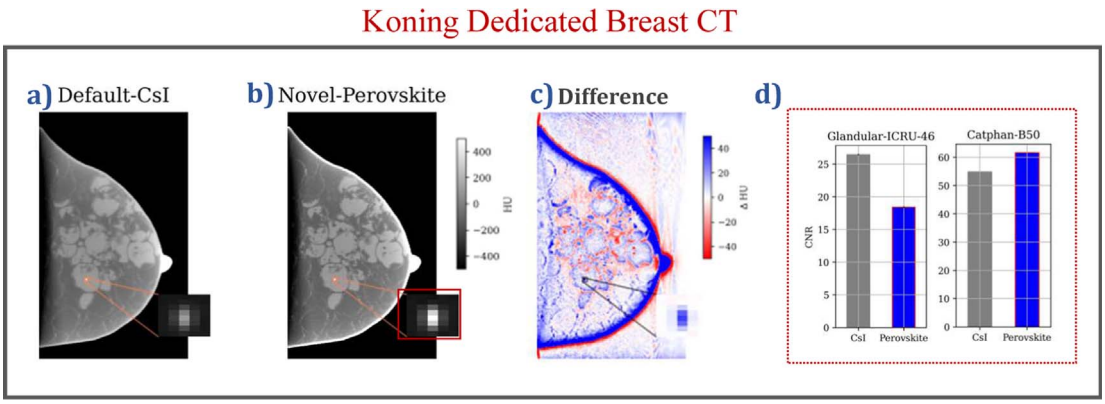

Figure 5. The results of the Koning BCT VCT are shown. (a)–(b) Images of the anthropomorphic breast phantom using CsI and Perovskite detectors with a microcalcification in the inlay. (c) The difference between CsI and Perovskite CBCTs, blue areas indicating regions where Perovskite has higher HU values. (d) CNR of key breast tissues for both detectors is plotted.

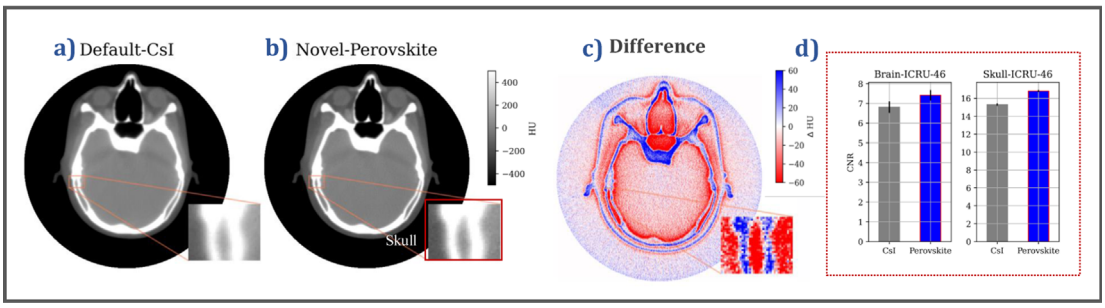

Figure 6. The results of the Truebeam kV-CBCT VCT are shown. (a)–(b) Images of the XCAT phantom's brain region using CsI and perovskite detectors, respectively, with fine bone features in the inlay. (c) The difference between CsI and perovskite CBCTs, blue areas indicating regions where perovskite has higher HU values. (d) CNR of key head tissues for both CBCTs are plotted.

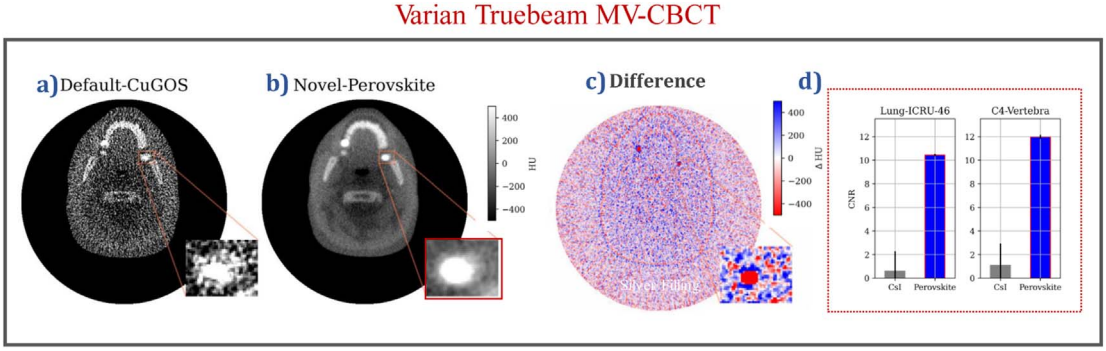

Figure 7. The results of the Varian MV-CBCT VCT are shown. (a)–(b) Images of the XCAT phantom's mandible region using GOS and Perovskite detectors, respectively, with silver amalgam fillings in the inlay. (c) The difference between GOS and Perovskite CBCTs, blue areas indicating regions where Perovskite has higher HU values. (d) CNR of key head tissues for both CBCTs are plotted.

detectors cannot be simulated easily in MC particle transport software. The presence of lead in the perovskite material resulted in the highest energy absorption in the mammography energy range. In the kV energy range, perovskite generally did not perform as well as other detector materials due to low EDE below the lead K-edge at 88 keV and poorer Compton absorption due to its relatively low density compared to the other detector materials. In the 0.5–1.5 MeV range which contains the majority of photons for MV imaging, the photo-electric attenuation of lead, due to its high atomic number led to greater EDE than all detectors save CZT.

One disadvantage of $MAPbBr_3$ perovskite crystals is the lower density as compared to CZT, GOS, and a-Se, as can be seen in table 1. When considering the degradation to spatial resolution incurred due to the detector

thickness, a higher density detector is advantageous as photons are attenuated more quickly in high density materials. The effect of the lower density would not be seen for mammography and breast CT applications as the x-rays do not travel far in the crystal due to the high photo-electric attenuation. However, for higher energy kV and MV beams, the more penetrating beams create geometric MTF degradation. For these cases higher density $MAPbI_3$ crystals would be advantageous and we estimate these crystals would be equivalent to CZT in terms of EDE in kV and MV applications, however it is yet to be seen if these crystals can be grown to the same thicknesses as $MAPbBr_3$ which we can grow to thicknesses of 15 mm in our lab. Another problem encountered with perovskites is that the lead containing crystals provide risk of toxicity if not encapsulated properly.

Care was taken to model detector physics in this work, however, there remain certain relevant detector parameters that were not feasible to model in this study. Without a pixelated perovskite detector we were unable to characterise the electronic noise and conversion efficiency in the detector and compare it to that of currently available detectors. Additionally, we did not include optimization of the current GOS and CsI detectors in this manuscript. This was partially based on the assumption that the crystal thickness was already optimised for their applications by the device manufacturer. Our goal was to compare this novel perovskite technology to existing detectors used in a clinical setting rather than to hypothetical devices. This does leave the possibility that there exist optimizations possible for CsI and GOS detectors to achieve similar DQE_r values given additional optimization.

Replacing the traditional GOS EPID with a novel-perovskite detector resulted in an improvement in DQE_r of 86.11%. This large improvement is due to a number of factors: GOS absorbs its own photon emissions, a property that limits the thickness of the GOS crystal. Likewise, GOS is a turbid phosphor, necessitating thin crystals to produce sharp images. The optimal GOS crystal thickness for the TrueBeam EPID scintillator is therefore a relatively thin 0.29 mm. Conversely, GOS is a convenient EPID material due to its radiation hardness that can withstand the therapeutic doses delivered routinely during linac quality assurance. It remains to be seen whether perovskite materials can provide sufficient radiation hardness for this application.

To allow for efficient optimization of crystal thickness, DQE_r was used as an optimization metric. While the use of a summary statistic such as DQE_r does not take into account the spatial information of the DQE, DQE_r is less noisy and contains more information than common metrics such as DQE_{10} or DQE_{50}. An obvious limitation of the DQE_r is that DQE at some spatial frequencies may be more important than others in some applications. For example, in breast microcalcification detection, high frequency DQE could be prioritised over low frequency DQE.

While detectors with pixel sizes less than 100 μm are used in medical imaging applications, the pixel size of the detectors discussed in this work was limited to 100 μm, as pixel pitch of less than 100 μm is uncommon in the CBCT applications discussed. In the case of the TrueBeam OBI, even the 194 μm pixels are regularly 2×2 binned to 388 μm during CBCT acquisition to decrease detector noise and speed up image reconstruction algorithms. From a manufacturing point of view, direct conversion detectors like perovskite materials can be manufactured with smaller pixel pitches than indirect conversion detectors and their application in fields like mammography will be a topic of future work.

A constraint on perovskite crystal thickness due geometric MTF degradation was introduced in this work. Specifically, in kV imaging, we find optimal detector thickness for perovskite to be 0.86 mm which is only slightly thicker than the 0.6 mm thickness often seen in CsI detectors. Perovskite detector's ability to produces high spatial resolution at large crystal thicknesses has a substantial 12.1% benefits to DQE over conventional detectors in Koning BCT and a 9.5% benefit to DQE in Truebeam kV-CBCT. Perovskite also provides greatly increased DQE in MV-CBCT imaging with a 87% increase over a GOS detector on a Truebeam machine. This could enable MV-CBCT to be used more routinely in clinical settings. Additionally, to truly maximise the benefit of thick perovskite detectors, applications such as PET imaging and CT imaging could be targeted; as the detector elements form a focused arc around the source reducing the distortion from geometric MTF degradation. Likewise, variable thickness in the detector or piece-wise focusing of the detector elements as in the work of Star-Lack *et al* (2015) could result in optimised DQE especially in MV imaging. Since the focal spot MTF degradation also effects the achievable DQE for these detectors, we also see potential for smaller focal spot x-ray tubes to be effective in increasing DQE even more than demonstrated here when used in combination with perovskite detectors especially for BCT.

5. Conclusion

Overall, perovskite-based x-ray detectors have high absorption efficiency and great spatial resolution at low production costs. Here we demonstrate device-specific systematic detector optimisation combined with a state-of-the-art VCT to present the impact of this technology in common medical x-ray imaging devices. We conclude that perovskite detectors perform better than current detectors in breast-CT and kV-CBCT

applications, and are far superior to current MV-CBCT detectors in terms of CNR and DQE. Future work aims implemented a prototype perovskite flat-panel detector on these specific devices for experimental verification of these VCT.

ORCID iDs

J O'Connell https://orcid.org/0000-0002-0548-4724

References

Bert J, Perez-Ponce H, Bitar Z E, Jan S, Boursier Y, Vintache D, Bonissent A, Morel C, Brasse D and Visvikis D 2013 Geant4-based monte carlo simulations on GPU for medical applications *Phys. Med. Biol.* **58** 5593–611

Capote R IAEA NDS 2023 www-nds.iaea.org/phsp/photon1/

Datta A, Fiala J and Motakef S 2021 2D perovskite-based high spatial resolution x-ray detectors *Sci. Rep.* **11** 22897

Dennis E, Kundu S, Thrithamarassery Gangadharan D, Huang J, Burlakov V M, Richtsmeier D, Bazalova-Carter M, Leitch D C and Saidaminov M I 2021 High length-to-width aspect ratio lead bromide microwiresviaperovskite-induced local concentration gradient for x-ray detection *Cryst. Eng. Comm.* **23** 2215–21

Dobbins J T, Samei E, Ranger N T and Chen Y 2006 Intercomparison of methods for image quality characterization: II. Noise power spectrum *Med. Phys.* **33** 1466–75

Dunning C A S, O'Connell J, Robinson S M, Murphy K J, Frencken A L, van Veggel F C J M, Iniewski K and Bazalova-Carter M 2020 Photon-counting computed tomography of lanthanide contrast agents with a high-flux 330 μm pitch cadmium zinc telluride detector in a table-top system *J. Med. Imaging* **7** 033502

Feldkamp L A, Davis L C and Kress J W 1984 Practical cone-beam algorithm *J. Opt. Soc. Am.* A **1** 612

Hernández G and Fernández F 2016 xpecgen: a program to calculate x-ray spectra generated in tungsten anodes *J. Open Source Software* **1** 11

Huang Y, Qiao L, Jiang Y, He T, Long R, Yang F, Wang L, Lei X, Yuan M and Chen J 2019 A-site cation engineering for highly efficient MAPbI3 single-crystal x-ray detector *Angew. Chem. Int. Ed.* **58** 17834

Jeon H, Youn H, Kim J S, Nam J, Lee J, Lee J, Park D, Kim W, Ki Y and Kim D 2017 Generation of polychromatic projection for dedicated breast computed tomography simulation using anthropomorphic numerical phantom *PLoS One* **12** 11

Kim Y C, Kim K H, Son D Y, Jeong D N, Seo J Y, Choi Y S, Han I T, Lee S Y and Park N G 2017 Printable organometallic perovskite enables large-area, low-dose x-ray imaging *Nature* **550** 87–91

López-Sánchez M, Pérez-Fernández M, Fandiño J M, Teijeiro A, Luna-Vega V, Gómez-Fernández N, Gómez F and González-Castaño D M 2019 An EGS monte carlo model for varian truebeam treatment units: commissioning and experimental validation of source parameters *Phys. Med.* **64** 81–8

Neitzel U, Maack I and Günther-Kohfah S 1994 Image quality of a digital chest radiography system based on a selenium detector *Med. Phys.* **21** 509–16

O'Connell J and Bazalova-Carter M 2021 fastCAT: fast cone beam CT (CBCT) simulation *Med. Phys.* **48** 4448–58

O'Connell J, Lindsay C and Bazalova-Carter M 2021 Experimental validation of Fastcat kV and MV cone beam CT (CBCT) simulator *Med. Phys.* **48** 6869–80

Papin P J and Huang H K 1987 A prototype amorphous selenium imaging plate system for digital radiography *Med. Phys.* **14** 322–9

Perl J, Shin J, Schumann J, Faddegon B and Paganetti H 2012 TOPAS: an innovative proton Monte Carlo platform for research and clinical applications *Med. Phys.* **39** 6818

Que W and Rowlands J A 1995 X-ray imaging using amorphous selenium: inherent spatial resolution *Med. Phys.* **22** 365–74

Ranger N T, Samei E, Dobbins J T and Ravin C E 2007 Assessment of detective quantum efficiency: intercomparison of a recently introduced international standard with prior methods *Radiology* **243** 785–95

Richtsmeier D, Dunning C A S, Iniewski K and Bazalova-Carter M 2020 Multi-contrast K-edge imaging on a bench-top photon-counting CT system: acquisition parameter study *J. Instrum.* **15** 10029

Rowlands J A, Hunter D M and Arai N 1991 X-ray imaging using amorphous selenium: a photoinduced discharge readout method for digital mammography *Med. Phys.* **18**

Safa Kasap P C 2017 *Springer Handbook of Electronic and Photonic Materials* (New York: Springer)

Segars W P, Sturgeon G, Mendonca S, Grimes J and Tsui B M W 2010 4D XCAT phantom for multimodality imaging research *Med. Phys.* **37** 4902–15

Shrestha S *et al* 2017 High-performance direct conversion x-ray detectors based on sintered hybrid lead triiodide perovskite wafers *Nat. Photon.* **11** 436–40

Star-Lack J *et al* 2015 A piecewise-focused high DQE detector for MV imaging *Med. Phys.* **42** 5084–99

Wei H *et al* 2016 Sensitive x-ray detectors made of methylammonium lead tribromide perovskite single crystals *Nat. Photon.* **10** 333–9

Woodard H Q and White D R 1986 The composition of body tissues *Br. J. Radiol.* **59** 1209–18

Yakunin S *et al* 2015 Detection of x-ray photons by solution-processed lead halide perovskites *Nat. Photon.* **9** 444–9

Ye F, Lin H, Wu H, Zhu L, Huang Z, Ouyang D, Niu G and Choy W C H 2019 High-quality cuboid CH3NH3PbI3 single crystals for high performance x-ray and photon detectors *Adv. Funct. Mater.* **29** 1806984